Spectrochimica Acta Part A: Molecular and Biomolecular Spectroscopy 149 (2015) 722–730

Contents lists available at ScienceDirect

Spectrochimica Acta Part A: Molecular and Biomolecular Spectroscopy

journal homepage: www.elsevier.com/locate/saa

Spectroscopic investigation, photophysical parameters and DFT calculations of 4,4′-(1E,1′E)-2,2′-(pyrazine-2,5-diyl)bis(ethene-2,1-diyl)bis(N,N-dimethylaniline) (PENDA) in different solvents

Abdullah M. Asiri [a,b], Khalid A. Alamry [a], Mehboobali Pannipara [a], Abdullah G. Al-Sehemi [c], Samy A. El-Daly [a,*]

[a] Department of Chemistry, Faculty of Science, King Abdulaziz University, P.O. Box 80203, Jeddah 21589, Saudi Arabia
[b] Center of Excellence for Advanced Materials Research, King Abdulaziz University, P.O. Box 80203, Jeddah 21589, Saudi Arabia
[c] Research Center for Advanced Materials Science (RCAMS), King Khalid University, P.O. Box 9004, Abha 61413, Saudi Arabia

HIGHLIGHTS

- New solvatochromic diolifinic dye.
- Highly photostable laser dye.
- DFT study.
- Fluorescence quenching by silver nanoparticle.

GRAPHICAL ABSTRACT

The graphical presentation of the highest occupied and lowest unoccupied molecular orbitals of title compound at B3LYP/6-31G* level of theory.

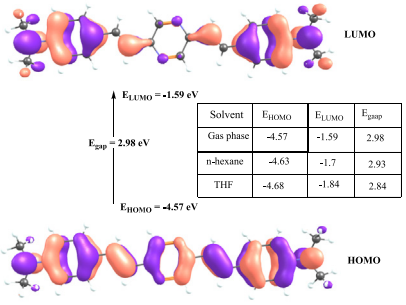

Solvent	E_{HOMO}	E_{LUMO}	E_{gap}
Gas phase	-4.57	-1.59	2.98
n-hexane	-4.63	-1.7	2.93
THF	-4.68	-1.84	2.84

ARTICLE INFO

Article history:
Received 11 February 2015
Received in revised form 22 April 2015
Accepted 4 May 2015
Available online 9 May 2015

Keywords:
Styryl pyrazine
Fluorescence quantum yield
Effect of solvent
DFT
Silver nanoparticles

ABSTRACT

A comprehensive investigation on the photophysics of a π-conjugated potential push–pull chromophore system 4,4′-(1E,1′E)-2,2′-(Pyrazine-2,5-diyl)bis(ethene-2,1-diyl)bis(N,N-dimethylaniline) (PENDA) has been carried out spectroscopically. The optical absorption and emission properties of this molecule have been studied in different solvents. The molecule PENDA shows strong solvatochromic emission upon changing the solvent polarity from nonpolar to polar; indicating that emission state is of intramolecular charge transfer (ICT) character. The solvent effect on the spectral properties such as singlet absorption, molar absorptivity, oscillator strength, dipole moment and fluorescence quantum yield of PENDA have been studied in detail. Lippert–Mataga and Reichardt correlations were used to estimate the difference between the excited and ground state dipole moments ($\Delta\mu$). Ground and electronic excited states geometric optimizations were performed using density functional theory (DFT) and time-dependent density functional theory (TDDFT), respectively, with the Gaussian 09 package. A solution of (8×10^{-5} M) PENDA in THF, dioxane, CH_3CN and $CHCl_3$ gives laser emission when pumped by a nitrogen laser pulse (λ_{ex} = 337.1 nm) of 800 ps duration and 1.48 mJ pulse energy. PENDA dye displays fluorescence

* Corresponding author at: King Abdulaziz University, P.O. Box 80302, Jeddah 21589, Saudi Arabia. Tel.: +966 554953522.
E-mail address: samyeldaly@yahoo.com (S.A. El-Daly).

http://dx.doi.org/10.1016/j.saa.2015.05.018
1386-1425/

quenching by colloidal silver nanoparticles (Ag NPs) in ethanol. The fluorescence data reveal that dynamic quenching and energy transfer play a major role in the fluorescence quenching mechanism.

Introduction

The development of new organic π-conjugated luminophores has been of great interest over the last few decades, due to their wide applications in various fields such as optoelectronics, bio-imaging, and optical storage devices [1–4]. Organic molecules containing both electron donating (D) and accepting (A) substituents in a single molecule exhibit interesting optical and spectral properties due to intramolecular charge transfer (ICT). This phenomenon led to substantial research owing to potential applications in photoelectronic and nonlinear optical devices [5,6], chemical sensing [7], and understanding photochemical and photobiological processes [8]. Compounds of this class show very strong solvent polarity dependent changes in their photophysical characteristics, specifically, large red shifts in their emission spectra with increasing solvent polarity, exceedingly high solvent polarity dependent changes in the Stokes shifts between absorption and fluorescence spectra, significant reduction in the fluorescence quantum yields (ϕ_f) and lifetimes (τ_f) on increasing the solvent polarity [9–11].

Organic molecules with large delocalised π-electron systems along their back bone have attracted significant interest due to potential applications associated with strong emission behaviour and large nonlinear optical properties [12–14].The presence and nature of electron-donating and electron-accepting groups play significant roles in such properties. Pyrazines [15], have nitrogen atoms at the 1, 4 positions of a six-membered aromatic ring. Due to their highly electron-withdrawing character, pyrazines are excellent candidates for incorporation as electron-withdrawing groups in push–pull scaffolds favouring intramolecular charge transfer (ICT). Diazines are of great importance since protonation, hydrogen-bond formation, and chelation through the nitrogen atoms of the heterocycle may be used for formation of supramolecular assemblies and therefore sensors.

Metallic nanoparticles due to their small size and high surface to volume ratios, possess unique spectroscopic, electronic and chemical properties that are different from those of the individual atoms as well as their bulk counterparts. The optical properties of noble metal nanoparticles have received considerable attention because the surface plasmon absorption band of noble metal nanoparticles appears in the visible region of the spectrum thus providing important contributions towards sensing and bio-medical applications [16,17]. Interaction of metallic nanoparticles (NPs) with fluorophores has been an active area of research over the last two decades with applications ranging from material to biomedical science [18,19]. The fluorescence of a dye molecule is quenched or enhanced in the close proximity of metallic nanoparticles and these phenomena can be used to probe the micro environment of the fluorophore. The emission behaviour of a dye can be altered by using metallic nanoparticles and quenching or enhancement of photoluminescence of a dye by silver nanoparticles (Ag NPs) depending upon the distance between the dye molecule and NPs [20–21]. The quenching processes are of three types: static, dynamic and by electron/energy transfer. In static quenching, the decrease in emission intensity is caused by adsorption of the dye on the surface of the metallic NPs, forming a non fluorescent complex between the fluorophore and quencher whereas in dynamic quenching, the reduction of emission intensity is due to direct interaction or collision of the excited fluorophore with a quencher during the excited state life time. The third type of quenching occurs by non-radiative energy/electron transfer between the dye molecule and NPs [22,23]. The quenching of fluorescence dominates over enhancement at shorter distances and it is attributed to the efficient non-radiative energy transfer between a dye and the metallic NP [23].

In continuation of our research in the area of synthesis and photophysical properties of organic molecules having donor–acceptor chromophores [24,25], we report here the spectral, and photophysical properties of a *D*-π-A-π-*D* type (where *D* is an electron-donating group, A an electron-accepting group, and π a conjugating moiety) in effect a linear styryl pyrazine bearing electron donating groups at opposite ends of the pyrazine core. The aim of the present work is to perform a detailed investigation on the spectral behaviours and photophysical properties of this donor–acceptor type styryl pyrazine derivative in different media. To explore the effect of metallic nanoparticles on the synthesized fluorophore, we also investigate fluorescence quenching by colloidal silver nanoparticles in ethanol using steady state emission measurements.

Experimental

Materials and methods

Spectroscopic grade solvents and chemicals were obtained from Sigma Aldrich and used without further purification. Silver nitrate, the metal precursor and the reducing agent trisodium citrate were used to prepare the silver nanofluid in doubly distilled water. Melting points were determined on a Gallenkamp melting point apparatus and infrared (IR) spectra were recorded on Shimadzu FT-IR 8400S infrared spectrophotometer using the KBr pellet technique. NMR (^{1}H and ^{13}C) spectra were recorded on a Bruker DPX-600 at 600 MHz and 150 MHz, respectively, using tetramethylsilane as the internal standard. The chemical shift values are

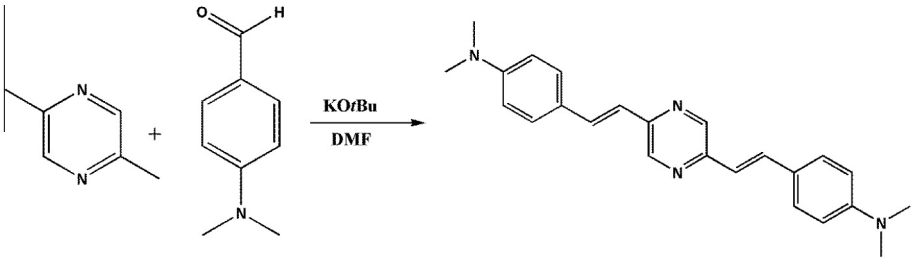

Scheme 1. The reaction of 2,5-dimethylpyrazine with 4-(dimethylamino)benzaldehyde.

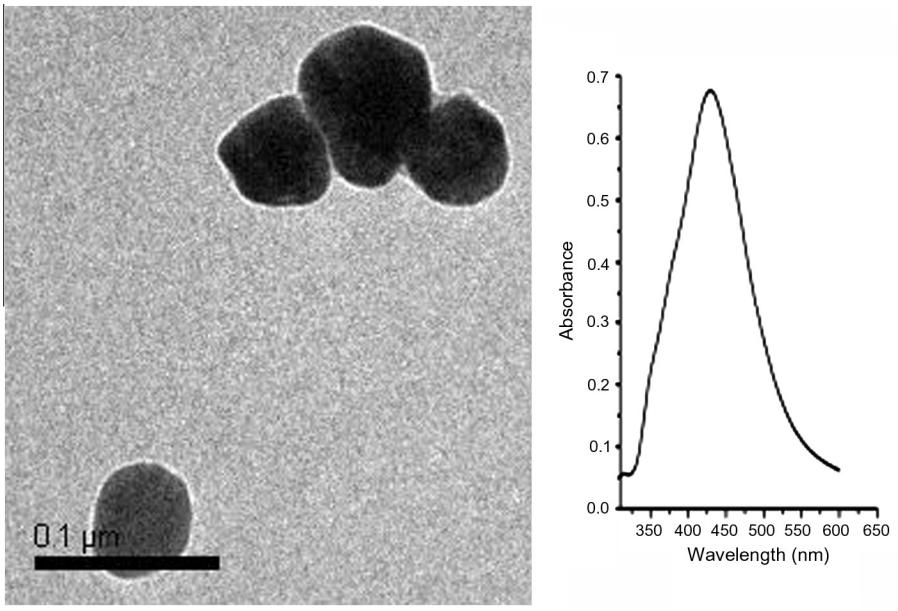

Fig. 1. TEM image and electronic absorption spectrum of Ag NPs (λ_{max} = 450 nm).

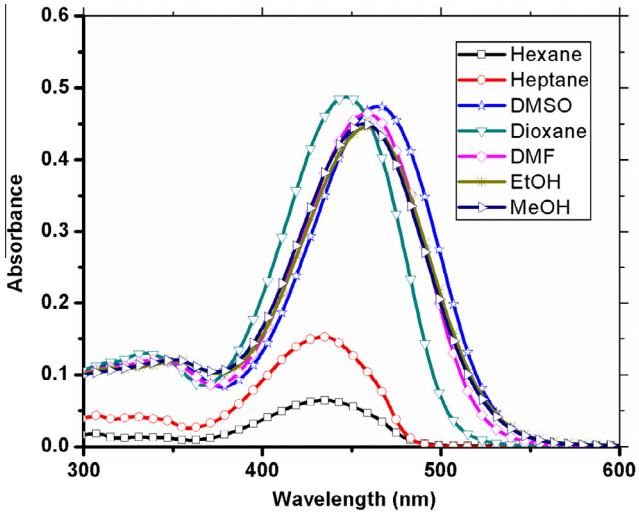

Fig. 2. Electronic absorption spectra of PENDA in different solvents.

recorded on δ scale and coupling constants (J) in Hz. Splitting patterns were designated as follows: *s*: singlet; *d*: doublet; *m*: multiplet. UV–Vis electronic absorption spectra was recorded on a Shimadzu UV-160A spectrophotometer, and the steady-state fluorescence spectra were measured using Shimadzu RF 5300 spectrofluorophotometer using a rectangular quartz cell of dimensions 0.2 cm × 3 cm. The emission was monitored at right angle. The fluorescence quantum yields (ϕ_f) in different solvents were measured using a comparative method where quinine sulfate (ϕ_f = 0.55 τ_f = 20 ns) in 0.5 M H_2SO_4 [26] solution was used as the reference according to Eq. (1):

$$\phi_u = \phi_s \times \frac{I_u}{I_s} \times \frac{A_s}{A_u} \times \frac{n_u^2}{n_s^2} \quad (1)$$

where ϕ_u, ϕ_s are the fluorescence quantum yields of the unknown and standard, respectively, I is the integrated emission intensity; A is the absorbance at excitation wavelength, and n is the refractive index of the solvent. The subscripts u and s refer to unknown and standard, respectively.

Procedure for the synthesis of 4,4′-(1E,1′E)-2,2′-(Pyrazine-2,5-diyl)bis(ethene-2,1-diyl)bis(N,N-dimethylaniline) (PENDA)

The title compound was synthesized by the reaction of 2,5-dimethylpyrazine with 4-(dimethylamino)benzaldehyde (Scheme 1). A solution of 2,5-dimethylpyrazine (0.5 g, 4.62 mmol) and the 4-(dimethylamino)benzaldehyde (2.3 g, 13 mmol) were dissolved in DMF and the mixture was cooled to 0 °C. To this mixture potassium-*tert*-butanolate (1.55 g, 13 mmol) was added in small portions and the mixture was brought to ambient temperature. Stirring was continued until all starting material had been consumed (TLC). After the completion of the reaction, water was added, and the product was isolated by extraction with chloroform. The organic layer was concentrated in vacuum and the solid material obtained was recrystallized to give the product (1.4 g, 52%) as a red solid. The structure of the compound was confirmed by IR, ^{1}H NMR and ^{13}C NMR.

^{1}H NMR ($CDCl_3$, 600 MHz): δ = 3.03 (s,12H), 6.74 (d,4H, J = 8.9 Hz), 6.94 (d,2H, J = 16.1 Hz), 7.49 (d,4H, J = 8.9 Hz), 7.64

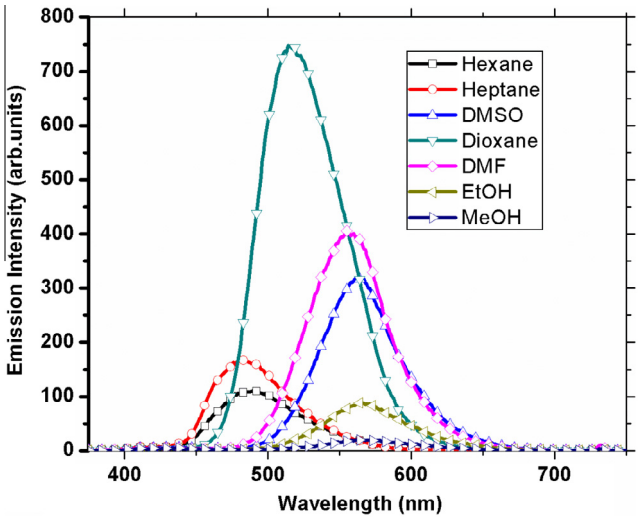

Fig. 3. Emission spectra of PENDA in different solvents (λ_{ex} = 380 nm).

Table 1
Spectral and Photophysical data of PENDA in different solvents.

Solvents	λ_{abs} (nm)	λ_{em} (nm)	$\Delta\bar{\nu}$ (cm^{-1})	ε M^{-1} cm^{-1}	Φ_f	f	μ_{12} Debye	$E_T(30)$ K cal mol^{-1}	Δf (D, n)	E_T^N
Hexane	434	492	2716	6480	0.64	0.11	3.16	31.1	0.0014	0.006
Toluene	450	514	2767	48,070	0.475	0.80	8.71	33.9	0.0132	0.099
Heptane	435	483	2285	15,280	0.38	0.26	4.91	31.1	0.0004	0.006
DMSO	464	562	3758	47,440	0.24	0.82	8.96	45.1	0.263	0.441
Dioxane	446	514	2966	48,770	0.55	0.83	8.86	36	0.021	0.164
THF	450	529	3319	45,150	0.45	0.77	8.55	37.4	0.210	0.210
Ethyl Acetate	445	523	3351	45,790	0.43	0.80	8.66	38.1	0.199	0.230
Acetonitrile	450	559	4333	49,830	0.27	0.88	9.17	45.6	0.304	0.472
Chloroform	457	548	3634	44,970	0.43	0.79	8.75	39.1	0.148	0.259
DMF	459	555	3768	46,420	0.31	0.79	8.78	43.8	0.274	0.404
Butanol	458	562	4040	44,270	0.19	0.79	8.78	50.2	0.263	0.506
Propanol	457	563	4120	44,240	0.15	0.79	8.72	49.2	0.274	0.570
Ethanol	458	565	4135	44,530	0.07	0.80	8.78	51.9	0.288	0.654
Methanol	457	566	4214	30,500	0.01	0.81	8.86	55.4	0.308	0.762

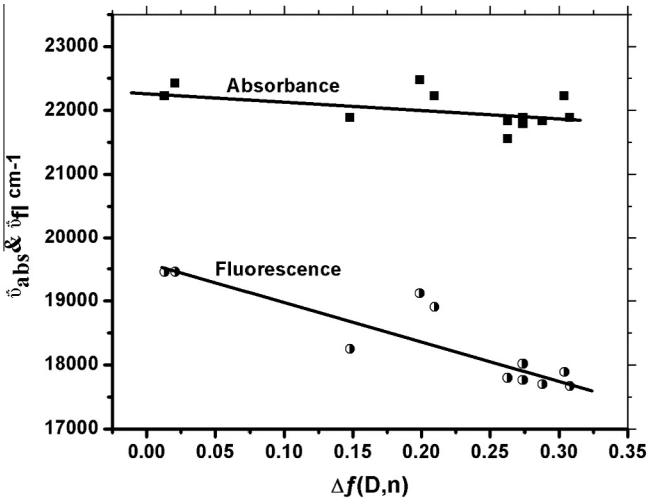

Fig. 4. Plot of energy of absorption and emission (Cm^{-1}) versus Δf of different solvents.

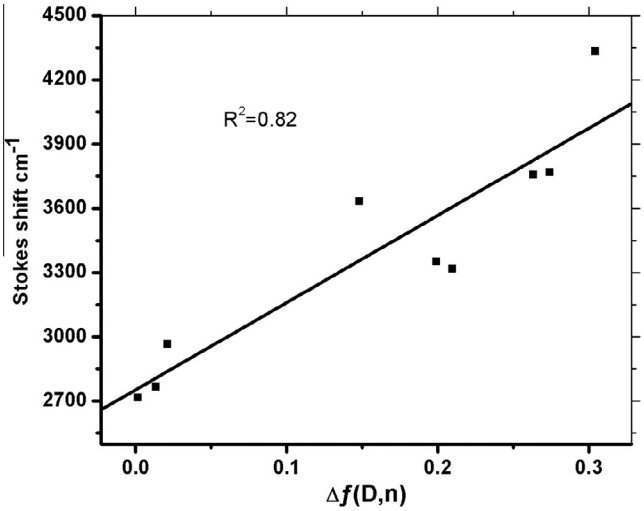

Fig. 5. Plot of Stokes shift of PENDA versus Δf (D, n) of different solvents.

(d,2H, J = 16.1 Hz), 8.49 (s,2H,). ^{13}C NMR (CDCl3, 150 MHz): δ = 40.3, 112.2, 120.7, 124.7, 127.5, 132.8, 141.7, 148.0, 150.7.

Synthesis and characterization of silver nanoparticles

Silver nanoparticles were prepared by a literature procedure [27]. In a typical preparation, 100 ml of 1×10^{-3} M silver nitrate solution was heated to boiling and 5 ml of 1% trisodium citrate solution (as nucleating and reducing agent) was added quickly, resulting in a color change from pale yellow to golden yellow indicating the formation of Ag NPs; stirring was continued until cooled to room temperature. The nanoparticles were characterized by UV–Vis absorption spectrophotometer and Transmission Electron Microscope (TEM). A typical solution of 40–45 nm diameter silver nanoparticles having polygonal shape, exhibiting a characteristic surface Plasmon band around 430 nm was obtained. A TEM image of Ag NPs with an absorption spectrum shown as an inset, is shown in Fig. 1.

Results and discussion

Solvent effect on absorption and emission spectra

The absorption and fluorescence spectra of (1×10^{-5} M) PENDA were recorded in solvents of different polarity. The absorption and emission spectra of PENDA in several solvents are shown in Figs. 2 and 3, and the corresponding spectral data are summarized in Table 1. As indicated in Fig. 2 and Table 1, absorption spectra of PENDA show a red shift of 30 nm on changing the solvent polarity from hexane to DMSO suggesting some polar character in the ground state. The red shift is expected in compounds having

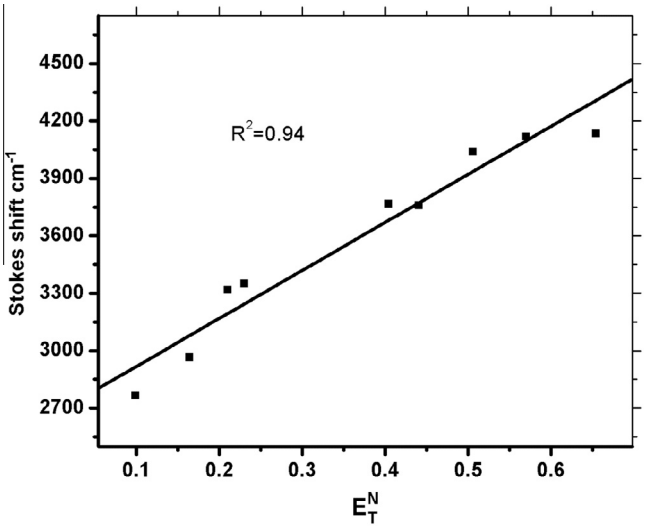

Fig. 6. Plot of Stokes shift (Cm^{-1}) versus normalized $E_T(30)$ of different solvents.

donor–acceptor groups in a single molecule and is due to strong intramolecular charge transfer (ICT) [28,29]. On excitation at 365 nm, the emission spectrum of PENDA correlates with increasing polarity of the solvent (Fig. 3). It is evident that the emission maxima undergo a red shift of 83 nm on increasing the polarity from heptane to methanol, suggesting the fluorescent state is more polar than the ground state. Thus the emission spectra are more sensitive to solvent polarity than the absorption spectra, which indicates that a larger charge transfer taking place in the excited state in comparison to the ground state, confirming the presence of π–π^* transitions in PENDA and stabilization of a highly dipolar excited state in polar solvents. The absorption and fluorescence peak energies (*abs* and *fl* respectively in cm-1) of PENDA has correlated with solvent polarity parameter Δf. As seen from Fig. 4, the *abs* and *fl* values follow reasonably good linear relationship with Δf and the plot between *fl* and Δf show large negative slop, indicating that the emission state is strongly dipolar in nature due to strong ICT from the donor to the acceptor moieties [30,31].

Estimation of dipole moments using solvatochromic methods

The solvatochromic method based on linear correlation between the absorption, fluorescence maxima and solvent polarity functions [32,33], is well-known for determining excited state and ground state dipole moment. Lippert–Mataga's Eqs. (2) and (3) [32,34], which is based on the correlation of energy difference between the ground and excited states (Stokes' shift) with the solvent orientation polarizability (Δf), can be used to investigate the change in dipole moment between the excited singlet state and ground state.

$$\Delta\bar{\nu}_{st} = \frac{2(\mu_e - \mu_g)^2}{hca^3}\Delta f + Const. \tag{2}$$

$$\Delta f = \frac{\varepsilon - 1}{2\varepsilon + 1} - \frac{n^2 - 1}{2n^2 + 1} \tag{3}$$

where $\Delta\bar{\nu}_{st}$ is the difference between the absorption and emission maxima expressed in wave numbers (cm^{-1}), respectively, h is Planck's constant, c is the speed of light in vacuum, a is the Onsager cavity radius, ε and n are the dielectric constant and refractive index of the solvent, respectively, μ_e and μ_g are the dipole moments in the excited and ground state, respectively, and Δf is the orientation polarizability of the solvent which measures both electron mobility and dipole moment of the solvent molecule. The Onsager cavity radius (a) from molecular volume of molecules is calculated using Suppan's Eq. (4) [35],

$$a = \left(\frac{3M}{4\pi\delta N}\right)^{1/3} \tag{4}$$

where δ is the density of dye, M is the molecular weight of dye and N is Avogadro's number. Fig. 5 shows the plot of Stokes shift versus the orientation polarization (Δf), The linear correlation of Lippert–Mataga plot supports the occurrence of photoinduced intramolecular charge transfer. The change in dipole moment calculated for PENDA from the slope of this plot and cavity radius (a) is found to be 5.47 D. The data in polar protic solvents were excluded from the plot of Fig 5, to avoid specific solute–solvent interactions (hydrogen bonding).

The change in dipole moment ($\Delta\mu$) between the excited singlet and ground state has been further investigated using the solvatochromic shift method introduced by Reichardt [36], making use of the dimensionless microscopic solvent polarity parameters E_T^N given by the Eqs. (5) and (6),

$$E_T^N = \frac{E_T(solvent) - 30.7}{32.4} \tag{5}$$

$$E_T(solvent) = \frac{28,591}{\lambda_{max}(nm)} \tag{6}$$

where λ_{max} corresponds to the peak wavelength in the red region of the intramolecular charge transfer absorption of the betaine dye. The main advantage of this method over the Lippert–Mataga method is the incorporation of hydrogen bonding in addition to the solvent polarity into the solvent parameter. In this method, change in dipole moment is calculated by correlating the Stokes shift of the fluorophore to E_T^N (Fig. 6) according to Eq. (7),

$$\Delta\bar{\nu} = 11307.6\left(\frac{\Delta\mu}{\Delta\mu_D}\right)^2\left(\frac{a_D}{a}\right)^3 E_T^N + Const. \tag{7}$$

where $\Delta\mu$ is the difference between the excited and ground state dipole moments of the probe molecule and $\Delta\mu_D$ is the change in the dipole moment of the betaine dye; a (taken as 4.34 Å) and a_D are the Onsager cavity radius of the probe molecule and betaine molecule, respectively. Since the values of a_D and μ_D are known (6.2 Å and 9 Debye, respectively) the change in dipole moment is calculated using Eq. (8),

$$\Delta\mu = \left[\frac{81m}{(6.2/a)^3 \times 11307.6}\right]^{1/2} \tag{8}$$

where, m is the slope of linear plot of E_T^N *vs* Stokes shift (Fig. 6) and the value of $\Delta\mu$ is found to be 5.58 D. The values of $\Delta\mu$ obtained by both methods are found to be very close and the higher value of $(\mu_e - \mu_g)$ suggests that the emissive state of PENDA is of strong ICT character.

The ground to excited state transition dipole moment (μ_{12}) of PENDA in different solvents was calculated using Eq. (9) [37]:

$$\mu_{12}^2 = \frac{f}{4.72 \times 10^{-7} E_{max}} \tag{9}$$

where E_{max} is the energy maximum absorption in cm^{-1} and f is the oscillator strength which shows the effective number of electrons whose transition from ground to excited state gives the absorption area of the electronic spectrum. The experimental oscillator strength values were calculated using Eq. (10) [38],

$$f = 4.32 \times 10^{-9} \int \varepsilon(\bar{\nu}) d\bar{\nu} \tag{10}$$

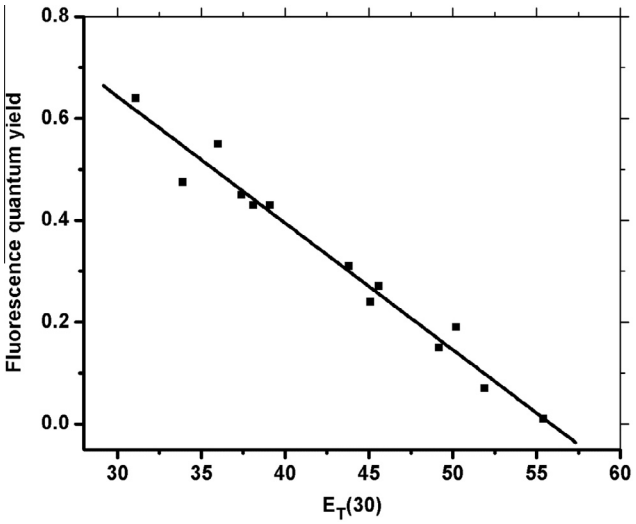

Fig. 7. Plot of fluorescence quantum yield of PENDA versus $E_T(30)$ of different solvents.

Table 2
Selected optimized geometrical parameters (bond length in Å and dihedral angle in °) and dipole moment (in Debye) computed for PENDA in gas phase and solvents at the ground (S_0) and first excited state (S_1) using B3LYP/6-31G*. For labeling, refer to Fig. 8.

	S0				S1			
	Gas phase	THF	*n*-hexane	Methanol	Gas phase	THF	*n*-hexane	Methanol
C_1–N_1	1.3266	1.3276	1.3055	1.3278	1.2978	1.3120	1.3128	1.3117
N_1–C_2	1.3555	1.3575	1.3487	1.3578	1.3985	1.3856	1.3810	1.3874
C_2–C_6	1.4566	1.4554	1.4543	1.4552	1.3910	1.4188	1.4227	1.4174
C_3–N_2	1.3266	1.3276	1.3054	1.3278	1.2978	1.3120	1.3128	1.3117
N_2–C_4	1.3555	1.3575	1.3486	1.3578	1.3984	1.3856	1.3810	1.3874
C_4–C_5	1.4566	1.4554	1.4544	1.4552	1.3910	1.4188	1.4227	1.4174
C_5–C_8	1.3531	1.3554	1.3507	1.3559	1.4161	1.3865	1.3820	1.3878
C_6–C_7	1.3531	1.3554	1.3509	1.3559	1.4161	1.3865	1.3820	1.3878
C_7–C_{10}	1.4574	1.4555	1.4559	1.4551	1.4274	1.4326	1.4354	1.4316
C_8–C_9	1.4574	1.4555	1.4562	1.4551	1.4274	1.4326	1.4354	1.4316
C_{13}–N_3	1.3855	1.3761	1.3796	1.3748	1.3852	1.3733	1.3781	1.3715
N_3–C_{22}	1.4531	1.4553	1.4536	1.4560	1.4535	1.4565	1.4541	1.4574
N_3–C_{21}	1.4527	1.4551	1.4532	1.4557	1.4532	1.4565	1.4540	1.4573
C_{18}–N_4	1.3854	1.3761	1.3823	1.3748	1.3852	1.3733	1.3781	1.3715
N_4–C_{23}	1.4527	1.4550	1.4541	1.4557	1.4531	1.4565	1.4540	1.4573
N_4–C_{24}	1.4531	1.4553	1.4545	1.4560	1.4534	1.4565	1.4541	1.4574
N_2–C_4–C_5–C_8	−179.8	−180.0	−180.0	−180.0	−179.9	−180.0	−180.0	−180.0
C_{20}–C_9–C_8–C_5	−179.7	−180.0	−180.0	−180.0	−180.0	−180.0	−180.0	−180.0
N_1–C_2–C_6–C_7	179.9	180.0	179.9	180.0	179.8	180.0	180.0	180.0
C_{15}–C_{10}–C_7–C_6	179.7	180.0	180.0	180.0	180.0	180.0	180.0	180.0
C_{12}–C_{13}–N_3–C_{21}	172.1	178.4	176.5	179.9	172.2	179.09	180.0	179.95
C_{12}–C_{13}–N_3–C_{22}	8.8	1.8	3.6	0.10	8.3	−0.07	0.005	0.061
C_{14}–C_{13}–N_3–C_{22}	−171.5	−178.3	−176.6	−179.9	−172.0	−179.9	−180.0	−179.9
C_{14}–C_{13}–N_3–C_{21}	−8.2	−1.7	−3.7	−0.09	−8.1	−0.11	−0.035	−0.056
C_{17}–C_{18}–N_4–C_{23}	−172.2	−178.5	−172.5	−179.9	−172.3	−179.9	−180.0	−179.93
C_{17}–C_{18}–N_4–C_{24}	−8.7	−1.6	−8.3	−0.12	−8.3	−0.06	−0.008	−0.073
C_{19}–C_{18}–N_4–C_{24}	171.6	178.5	172.0	179.9	172.1	179.9	180.0	179.93
C_{19}–C_{18}–N_4–C_{23}	8.2	1.5	7.7	0.12	8.1	0.10	0.037	0.073

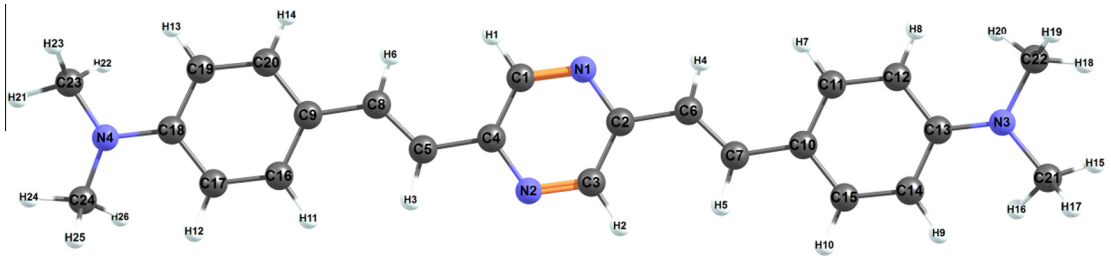

Fig. 8. The optimized molecular structure of PENDA compound.

where ε is the numerical value for molar absorption coefficient measured in $dm^3\ mol^{-1}\ cm^{-1}$ and $\bar{\nu}$ is the numerical value of the wave number measured in cm^{-1}. The values of f and μ_{12} are listed in Table 1 and indicate that the $S_o \rightarrow S_1$ transition is the allowed transition.

Fluorescence quantum yield of PENDA in different solvents

The fluorescence quantum yield (ϕ_f) of PENDA is strongly influenced by the polarity and hydrogen bonding ability of the solvent (Table 1). As shown in Table 1, the value of ϕ_f decreases with increasing solvent polarity $E_T(30)$, where $E_T(30)$ is the solvent polarity parameter that considers interactions such as solvent polarizability and hydrogen bonding besides those of a specific nature. This could be attributed to efficient internal conversion and/or intersystem crossing by extensive mixing between the close – lying $^1(\pi$–$\pi^*)$ and $^1(n - \pi^*)$ states. In addition the non-radiative rate increases markedly in solvents with strong hydrogen bond character such as alcoholic solvents and competes with fluorescence emission due to the enhancement of intersystem crossing, strong internal conversion and vibrational deactivation. The fluorescence quantum yield of PENDA in different solvents is correlated with the empirical Dimroth polarity parameters $E_T(30)$ of solvent (Fig. 7). A linear correlation was obtained, implying potential application of PENDA to probe the polarity of the medium [11,39–42]. The decrease in ϕ_f (positive solvatokinetic effect) in highly polar protic solvents is because the photoexcited dye with ICT state undergoes a conversion to a highly polar TICT state by twisting of the molecule around a C–C single bond, making a complete transfer of electrons from donor to acceptor moiety.

Theoretical calculations

The ground and electronic excited states geometric optimizations of PENDA are performed using density functional theory (DFT) and time-dependent density functional theory (TDDFT) methods, respectively, with the Gaussian 09 package [43]. The DFT was treated according to Becke's three parameter gradient-corrected exchange potential and the Lee–Yang–Parr gradient-corrected correlation potential (B3LYP) [44–46], and all calculations were performed by using 6-31G* basis set [47]. This model has been widely used for geometry optimization and the determination of electronic properties [24]. TDDFT has been used to investigate absorption spectra and has proved to be an efficient

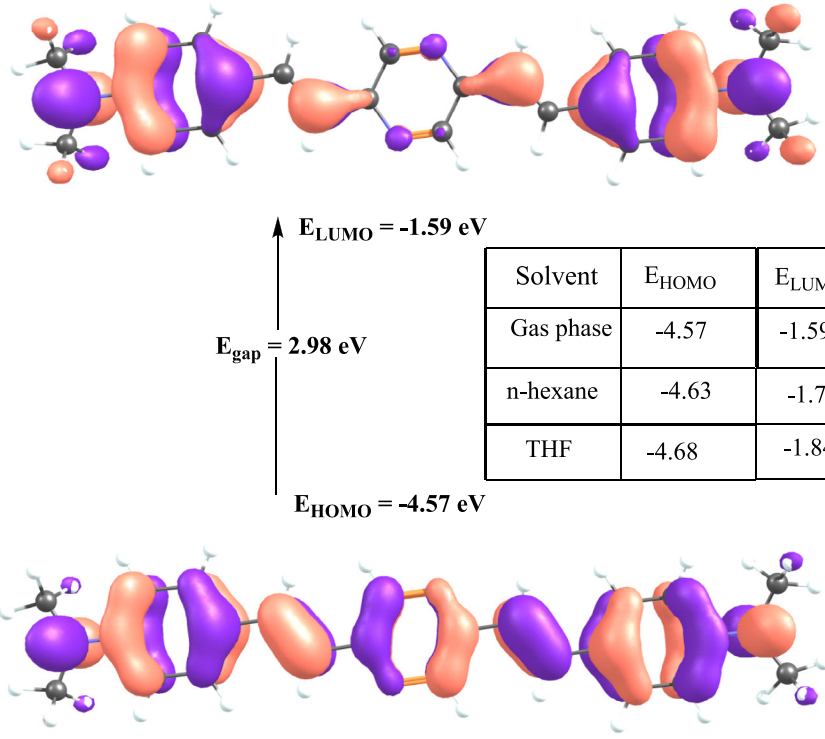

Solvent	E_{HOMO}	E_{LUMO}	E_{gaap}
Gas phase	-4.57	-1.59	2.98
n-hexane	-4.63	-1.7	2.93
THF	-4.68	-1.84	2.84

Fig. 9. The graphical presentation of the highest occupied and lowest unoccupied molecular orbitals of title compound at B3LYP/6-31G* level of theory.

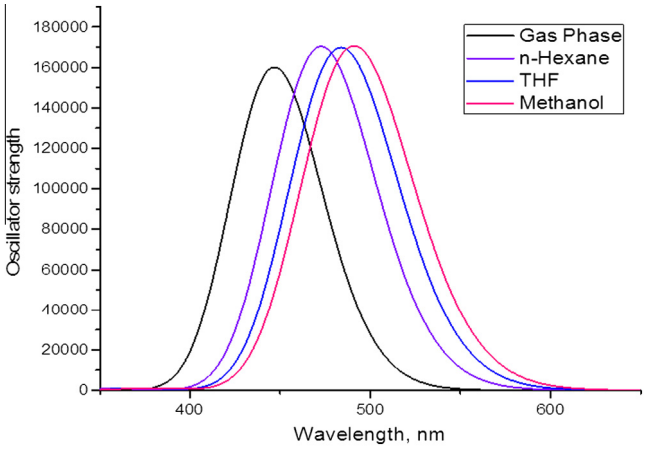

Fig. 10. Calculated absorption spectrum of PENDA in gas phase (in black), *n*-hexane (in purple), THF (in blue) and methanol (in red). (For interpretation of the references to colour in this figure legend, the reader is referred to the web version of this article.)

approach [48–50]. The polarizable continuum model (PCM) [51,52] was used for evaluating bulk solvent effects at all stages. The PCM-TDB3LYP/6-31G* level of theory was used to compute the absorption spectra in THF, *n*-hexane and methanol.

The geometrical parameters of the ground and excited states are presented in Table 2. The labeling scheme is shown in Fig. 8. We applied the DFT method to obtain the ground state geometrical and electronic structure of PENDA in the gas phase (as a control) and in solvents. The dielectric constants used in the PCM calculation are the default values in GAUSSIAN 09. We use PCM with *n*-hexane ($\varepsilon = 1.882$) and tetrahydrofuran (THF) ($\varepsilon = 7.426$) and methanol ($\varepsilon = 32.613$) as solvents. TD-DFT was used to investigate the excited state properties in the gas phase and solvents, together with the 6-31G(d). The optimized values of bond lengths and bond/dihedral angles for the structures are tabulated in Table 2. In general, N1–C2, N2–C4, C5–C8, C6–C7, N3–C21, N3–C22, N4–C23 and N4–C24 bond lengths increase from ground state to excited state for all solvents used and the difference value 0.032, 0.032, 0.035, 0.035, 0.0043, 0.0046, 0.0046 and 0.0043 Ã respectively. On the other hand, C1–N1, C2–C6, C3–N3, C4–C5, C7–C10, C8–C9, C13–N3 and C18–N24 bond lengths shortened from ground to excited states, i.e., 0.015, 0.039, 0.015, 0.039, 0.026, 0.026, 0.014 and 0.014 Ã, respectively.

In the PENDA molecule, the two benzene rings attached to the pyrazine ring with bridge are planar and have dihedral angles of $N_1–C_4–C_5–C_8$, $C_{20}–C_9–C_8–C_5$, $N_1–C_2–C_6–C_7$ and $C_{15}–C_{10}–C_7–C_6$, between 179.7 to 180.0 in both ground and excited states Table 2. Fig. 9 illustrates the frontier molecular orbital, highest occupied molecular orbitals (HOMO) and lowest unoccupied

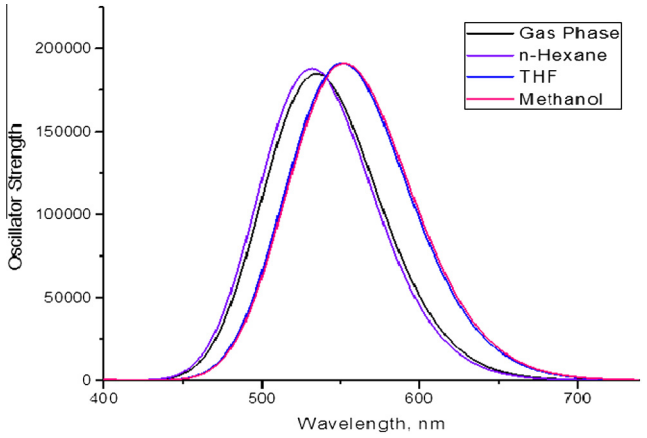

Fig. 11. Calculated emission spectrum of PENDA in gas phase (black), *n*-hexane (purple), THF (blue) and methanol (red). (For interpretation of the references to colour in this figure legend, the reader is referred to the web version of this article.)

Table 3
Photophysical parameters of laser emission of PENDA in some solvents.

Solvent	$\lambda_{ex(max)}$	Tuning range (nm)	Gain coefficient (α) cm^{-1}
THF	514	482–562	1.42
Dioxane	548	482–572	1.25
$CHCl_3$	529	505–590	1.25
CH_3CN	558	514–604	1.02

molecular orbitals (LUMO). The HOMO is π bonding while the LUMO is of antibonding character with π^* distributed over the whole molecule. The HOMO is delocalized over the whole molecule and the lone pair of electrons on the nitrogen atoms. The HOMO–LUMO energy gap of this compound was calculated at the B3LYP/6-31G* level of theory, (Fig. 9). Orbital energy level analysis at the B3LYP/6-31G* level and the resultant HOMO–LUMO energy gap (E_{gap}) has been used as an indicator of kinetic stability of a molecule. A large HOMO–LUMO gap implies a high kinetic stability and low chemical reactivity, because it is energetically unfavourable to add electrons to a high-lying LUMO or to remove electrons from a low-lying HOMO. As shown in Fig. 9 the HOMO is delocalized over the whole of the molecule; the four nitrogen atoms also take part in the HOMO. The LUMOs are also distributed over the whole of the molecule, but the pyrazine ring core contribution to the LUMO is small. We also computed the HOMO–LUMO orbitals energy and energy gap at the same level of theory in gas phase, *n*-hexane and THF. In the solvent, THF lowers the HOMO and LUMO energies by about 0.11–0.25 eV and *n*-hexane decreases the HOMO and LUMO energies from 0.047 to 0.14 eV respectively. The effect of solvents on the HOMO–LUMO energy gap are also shown in Fig. 9, the larger E_{gap} in THF revealing that the spectrum would be red shifted.

In order to study the effect of solvents on the ground and excited states, quantum chemical calculations were carried out in gas phase (as a control), *n*-hexane, tetrahydrofuran (THF) and methanol using the TDDFT/PCM method. The UV–Vis absorption spectra of PENDA exhibit only one band of maximum absorption between 446.6 and 490.7 nm, depending on the solvent, whereas the corresponding emission values occur between 531and 552 nm, (Figs. 10 and 11). There is a gradual increase in the calculated properties with an increase in dielectric constant of the solvents. In addition, computed absorptions attain 2.776, 2.624, 2.564 and 2.527 eV, whereas the corresponding emission values are 2.321, 2.334, 2.251 and 2.246 eV. The emission maximum wavelength (λ_{max}) shows a red shift relative to the absorption λ_{max} as the polarity of the solvent strengthens. The pronounced shift in the emission spectra is an indication of a $\pi \rightarrow \pi^*$ transition. The calculated absorption and emission spectra are in excellent agreement with experimental observation.

Laser activity of PENDA

A solution of PENDA (8×10^{-5} M) in THF, dioxane, CH_3CN and $CHCl_3$ gave laser emission when pumped by a nitrogen laser pulse (λ_{ex} = 337.1 nm) of 800 ps duration and 1.48 mJ pulse energy. The solutions were placed in oscillator and amplifier cuvettes of 10 mm path length. The output energy of the laser dye was measured as a function of wavelength to determine the lasing range in different solvents. The dye gave laser emission at fluorescence maximum comparable to steady state emission maximum. The maximum gain coefficient (α) was calculated at maximum laser emission by measuring the intensity I_L of laser emission over the entire cell length L and the intensity over half the cell length $I_{L/2}$. The laser gain emission was calculated using Eq. (11) [53],

$$\alpha(\lambda) = \frac{2}{L} \ln \left[\frac{I_L}{I_{L/2}} - 1 \right] \quad (11)$$

Table 3 summarizes the laser emission data of dye in different solvents. It is well known that gain occurs when the stimulated emission of photons exceeds the re-absorption or loss due to scattering. Hence, gain is the increase in the number of emitted photons and is dependent on both wavelength and incident intensity.

Fluorescence quenching study of PENDA by silver nanoparticles

Quenching studies can be used as a tool to investigate response of fluorophores to quenchers and hence the nature of molecular interaction and microenvironment of fluorophores in solution can be studied by fluorescence quenching experiments. Fluorescence measurements were performed to investigate the interaction of silver nanoparticles with PENDA with variable concentrations of Ag NPs in ethanol. The emission spectra (1×10^{-5} M) of PENDA in ethanol at different concentrations of Ag NPs are shown in Fig. 12. The emission spectrum of PENDA remains unaltered in wavelength but a substantial decrease in

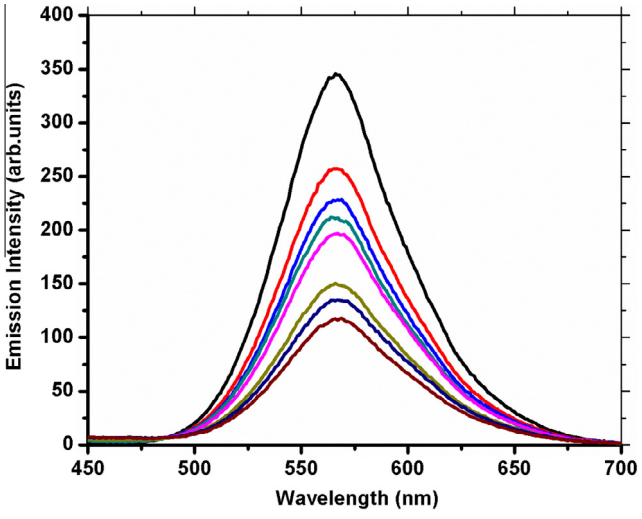

Fig. 12. Emission spectra of 1×10^{-5} M of PENDA in ethanol at different concentrations of Ag NPS. The concentrations of Ag Nps at decreasing emission intensity are 0.0, 0.039, 0.0 78, 0.117, 0.156, 0.195, 0.273 and 0. 312 nM (λ_{ex} = 340 nm).

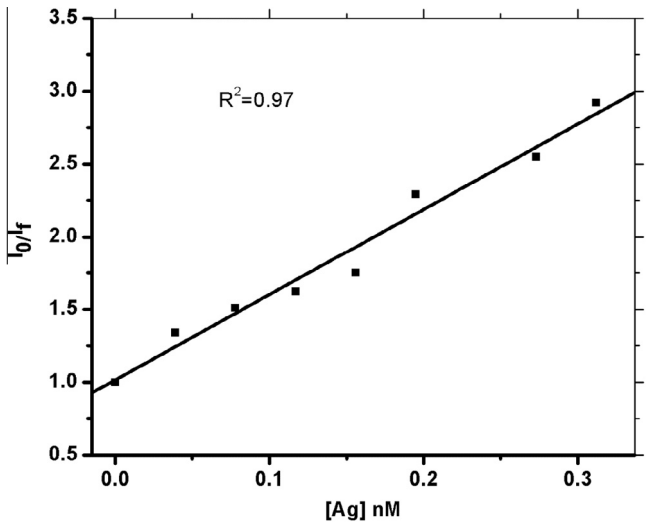

Fig. 13. Stern–Volmer plot for fluorescence quenching of PENDA by Ag NPs in ethanol.

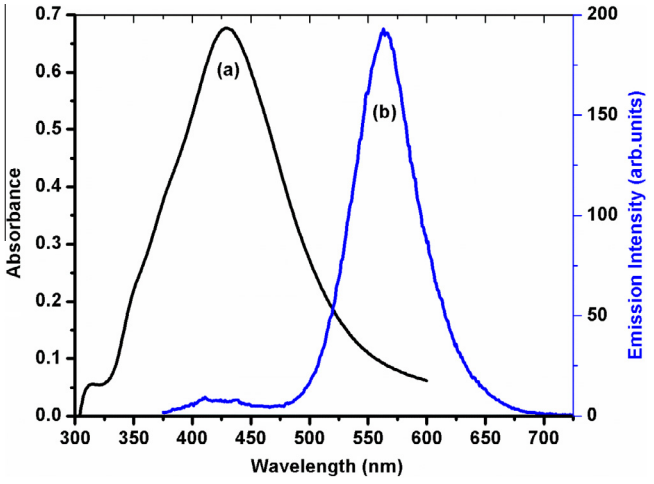

Fig. 14. Shows the spectral overlap of (a) absorption of Ag Nps with (b) emission spectrum of PENDA in ethanol.

fluorescence intensity was observed on increasing the concentration of Ag NPs which rules out the possibility of ground state complex formation between PENDA and Ag NPs.

The fluorescence quenching behaviour can be analyzed by the Stern–Volmer Eq. (12) to determine the Stern–Volmer quenching constant (K_{sv}) for PENDA using Ag NPs as quencher [30]:

$$\frac{I_o}{I} = 1 + K_{sv}[Ag^o] \tag{12}$$

where I_o and I are the fluorescence intensities in the absence and presence of the quencher concentration [Ag^o]. The Stern–Volmer plot for PENDA (Fig. 13) was found to be linear with correlation $R^2 = 0.97$ in ethanol and the K_{sv} value calculated from the slope of the linear plot was found to be $5.86 \times 10^9\ M^{-1}$. The significant overlap between the emission spectrum of PENDA and the absorption of spectrum of Ag NPs (Fig. 14) reveal the possibility of radiative radiative energy transfer from excited PENDA to ground state Ag NPs, non-radiative energy transfer is also possible according to Förster's theory [54]. Thus, the Stern–Volmer plot and the spectral overlap between the PENDA and Ag NPs indicate the dynamic nature and radiative energy transfer of the quenching process.

Conclusion

A styryl pyrazine derivative (PENDA) having *D*-π-A-π-*D* type structure has been synthesized and characterized by spectroscopic methods. The photophysical properties were investigated in protic and aprotic solvents. It is inferred from the absorption and emission spectra that emissive state of PENDA has intramolecular charge transfer characteristics. The fluorescence quantum yield (ϕ_f) of PENDA is strongly influenced by the polarity and hydrogen bonding ability of the solvents and ϕ_f undergoes a sharp decrease with increasing the polarity of the solvent. Further, from the Lippert–Mataga and Reichardt correlations it is found that photoinduced intramolecular charge transfer (ICT) occurs in the excited state and the polarity of the dye increases on excitation. The calculated absorption and emission spectra are in excellent agreement with experimental observation. The interactions of PENDA with colloidal silver nanoparticles in ethanol have also been studied using fluorescence techniques. Fluorescence quenching data suggest that radiative energy transfer from excited PENDA to ground state Ag NPs play major roles in the fluorescence quenching process.

References

[1] A.C. Grimsdale, K.L. Chan, R.E. Martin, P.G. Jokisz, A.B. Holmes, Chem. Rev. 109 (2009) 897–1091.
[2] D. Braga, G. Horowitz, Adv. Mater. 21 (2009) 1473–1486.
[3] R.J. Radford, W. Chyan, S.J. Lippard, Chem. Sci. 4 (2013) 3080–3084.
[4] A. Facchetti, Chem. Mater. 23 (2011) 733–758.
[5] A.C. Arias, J.D. MacKenzie, I. McCulloch, J. Rivnay, A. Salleo, Chem. Rev. 110 (2010) 3–24.
[6] K.M. Rahulan, S. Balamurugan, K.S. Meena, G.-Y. Yeap, C.C. Kanakam, Opt. Laser Technol. 56 (2014) 142–145.
[7] H. Singh, J. Sindhu, J.M. Khurana, Sens. Actuators, A 192 (2014) 536–542.
[8] Z.R. Grabowski, K. Rotkiewicz, W. Rettig, Chem. Rev. 103 (2003) 3899–4302.
[9] T.H.N. Pham, R.J. Clarke, J. Phys. Chem. B 112 (2008) 6513.
[10] Y. Huang, T. Cheng, F. Li, C. Huang, T. Hou, A. Yu, X. Zhao, X. Xu, J. Phys. Chem. B 106 (2002) 10020.
[11] M. Shaikh, J. Mohanty, P.K. Singh, A.C. Bhasikuttan, R.N. Rajule, V.S. Satam, S.R. Bendre, V.R. Kanetkar, H. Pal, J. Phys. Chem. A 114 (2010) 450.
[12] H.N. Kim, Z. Guo, W. Zhu, J. Yoon, H. Tian, Chem. Soc. Rev. 40 (2011) 79–93.
[13] G.S. He, L.-S. Tan, Q. Zheng, P.N. Prasad, Chem. Rev. 108 (2008) 1245–1330.
[14] Z. Li, Q. Li, J. Qin, Polym. Chem. 2 (2011) 2723–2740.
[15] R.N. Castle, Chemistry of Heterocyclic Compounds, vol. 23, John Wiley and Sons, New York, 1962.
[16] B. Hong, K.A. Kang, Biosens. Bioelectron. 21 (2006) 1333.
[17] M.Y. Ng, W.C. Liu, Opt. Express 17 (2009) 5867.
[18] M.C. Daniel, D. Astruc, Chem. Rev. 104 (2004) 293.
[19] W. Deng, E.M. Goldys, Langmuir 28 (2012) 10152.
[20] Y. Fu, J. Zhang, J.R. Lakowicz, J. Fluoresc. 17 (2007) 811.
[21] S. Kalele, A.C. Deshpande, S.B. Singh, S.K. Kulkarni, Bull. Mater. Sci. 31 (2008) 541.
[22] N. Shemeena Basheer, B. Rajesh Kumar, Achamma Kurian, Sajan D. George, J. Lumin. 137 (2013) 225–229.
[23] S. Pushpam, M. Kottaisamy, V. Ramakrishnan, Spectrochim. Acta, Part A 114 (2013) 272–276.
[24] S.A. El-Daly, A.M. Asiri, M.A. Hussein, A.G. Sehemi, J. Luninescence 148 (2014) 317–324.
[25] S.A. El-Daly, E.M. Ebeid, J. Mol. Struct. 1063 (2014) 213–218.
[26] K.P. Ghiggino, P.F. Skilton, P.J. Thistlethwaite, J. Photochem. 31 (1985) 113–121.
[27] P.C. Lee, D. Meisel, Adsorption and surface-enhanced Raman of dyes on silver and gold sols, J. Phys. Chem. 86 (17) (1982) 3391–3395.
[28] P. Dahiya, D.K. Maity, S.K. Nayak, T. Mukherjee, H. Pal, J. Photochem. Photobiol., A 186 (2007) 218.
[29] P. Dahiya, M. Kumbhakar, T. Mukherjee, H. Pal, J. Mol. Struct. 798 (2006) 40.
[30] J.R. Lakowicz, Principle of Fluorescence Spectroscopy, Plenum Press, New York, 2006.
[31] P. Dahiya, S. Dutta Choudhury, D.K. Maity, T. Mukherjee, H. Pal, Spectrochim. Acta A 69 (2008) 134.
[32] E. Lippert, Z. Naturforsch. 10 (1955) 541–545.
[33] A. Chamma, P. Viallet, C.R. Acad. Sci., Ser. C 270 (1970) 1901–1910.
[34] N. Mataga, T. Kubota, Molecular Interactions and electronic spectra, Marcel Dekker New York (1970) 371–410.
[35] P. Suppan, Chem. Phys. Lett. 94 (1983) 272.
[36] C. Reichardt, Chem. Rev. 94 (1994) 2319–2358.
[37] B.J. Coe, J.A. Harris, I. Asselberghs, K. Clays, G. Olbrechts, A. Persoons, J.T. Hupp, R.C. Johnson, S.J. Coles, M.B. Hursthouse, K. Nakatani, Adv. Funct. Mater. 12 (2002) 110–116.
[38] P. Gordon, P. Gregory, Organic Chemistry in Colour, Chimia, Moskva, 1987.
[39] T. Shim, M.H. Lee, D. Kim, Y. Ouchi, J. Phys. Chem. B 112 (2008) 1906.
[40] J.B. Birks, Organic Molecular Photophysics, John Wiley and Sons, New York, 1973.
[41] S.A. El-Daly, A.M. Asiri, S.A. Khan, K.A. Alamry, J. Lumin. 134 (2013) 819–824.
[42] S. Jana, S. Dalapati, S. Ghosh, N. Guchhait, J. Photochem. Photobiol., A 261 (2013) 31–40.
[43] M.J. Frisch et al., Gaussian 09, Revision B 4, Gaussian Inc., Pittsburg, PA, 2003.
[44] A.D. Becke, J. Chem. Phys. 98 (1993) 5648.
[45] B. Miehlich, A. Savin, H. Stoll, H. Preuss, Chem. Phys. Lett. 157 (1989) 200.
[46] C. Lee, W. Yang, R.G. Parr, Phys. Rev. B 37 (1988) 785.
[47] J. Sun, J. Song, Y. Zhao, W.Z. Liang, J. Chem. Phys. 127 (2007) 234107.
[48] S.A. El-Daly, A.M. Asiri, K.A. Alamry, A.G. Al-Sehemi, J. Mol. Struct. 1037 (2013) 323–331.
[49] C.R. Zhang, W.Z. Liang, H.S. Chen, Y.H. Chen, Z.Q. Wei, Y.Z. Wu, J. Mol. Struct. (THEOCHEM) 862 (2008) 98.
[50] D. Matthews, P. Infelta, M. Grätzel, Sol. Energy Mater. Sol. Cells 44 (1996) 119.
[51] M. Cossi, V. Barone, J. Chem. Phys. 115 (2001) 4708.
[52] C. Amovilli, V. Barone, R. Cammi, E. Cancès, M. Cossi, B. Mennucci, C.S. Pomelli, J. Tomasi, Adv. Quant. Chem. 32 (1998) 227.
[53] M. Rink, H. Gusten, H.J. Ache, Phys. Chem. 90 (1986) 2661–2665.
[54] T. Förster, in: O. Sinanoglu (Ed.), Modern Quantum Chemistry, Academic Press, New York, 1996.